

High-efficiency and broadband photonic polarization rotator based on multilevel shape optimization

Nicolas Lebbe, Alain Gliere, Karim Hassan

▶ **To cite this version:**

Nicolas Lebbe, Alain Gliere, Karim Hassan. High-efficiency and broadband photonic polarization rotator based on multilevel shape optimization. Optics Letters, 2019, 44 (8), pp.1960-1963. 10.1364/OL.44.001960 . cea-02091228

HAL Id: cea-02091228
https://cea.hal.science/cea-02091228

Submitted on 5 Apr 2019

HAL is a multi-disciplinary open access archive for the deposit and dissemination of scientific research documents, whether they are published or not. The documents may come from teaching and research institutions in France or abroad, or from public or private research centers.

L'archive ouverte pluridisciplinaire **HAL**, est destinée au dépôt et à la diffusion de documents scientifiques de niveau recherche, publiés ou non, émanant des établissements d'enseignement et de recherche français ou étrangers, des laboratoires publics ou privés.

High efficiency and broadband photonic polarization rotator based on multi-level shape optimization

NICOLAS LEBBE[1,2], ALAIN GLIÈRE[1], AND KARIM HASSAN[1,*]

[1] Univ. Grenoble Alpes, CEA, LETI, F38000 Grenoble, France
[2] Univ. Grenoble Alpes, LJK, F38000 Grenoble, France
[*] Corresponding author: karim.hassan@cea.fr

Compiled March 20, 2019

We report on a novel photonic polarization rotator design obtained by multi-level shape optimization. The numerical method consists in a topological optimization scheme improving iteratively the efficiency of the component by modifying its shape on two discrete levels along the etching direction. We numerically show that, compared to the state of the art single level shape optimization, the performances can be drastically improved for a given device length. Next, the polarization conversion efficiency can be further improved up to a computed value of ~98.5 % with less than 0.35 dB insertion losses on a 100 nm bandwidth for a 6 µm × 1 µm footprint. © 2019 Optical Society of America

http://dx.doi.org/10.1364/ao.XX.XXXXXX

1. INTRODUCTION

Integrated polarization rotator on chip have been extensively investigated during the last decades. This photonics component is of key interest for numerous applications, from telecommunication [1–3] to sensing [4], and optical quantum computing [5]. Efficiency and compactness of such a device remain of great importance in order to follow the growing needs in term of scalability for optical transceivers, requiring every year higher bandwidths and lower insertion losses. Silicon photonics has proven its strength for active and passive devices up to industrial products [6]. Ultra-compact silicon photonic elements were recently demonstrated thanks to disruptive computation methods known as inverse design or shape optimization [7–9]. However the compactness of those non-intuitive designs is often limited by the resulting insertion losses. While some power penalty can be accepted for specific functions used locally – for instance multiplexers used once per chip – insertion losses of other functions implemented repeatedly must be minimized. One can note that alternatively, plasmonic and hybrid photonic-plasmonic devices were also proposed to improve the compactness of on-chip functions, at the expense of relatively high insertion losses due to the close proximity of the metal layers [10, 11].

To the best of our knowledge, state of the art photonic polarization rotator obtained by inverse design have been demonstrated in Ref [12]. While good performances were obtained through a binary optimization, the polarization conversion seems limited by the vertically invariant design. It is well-known that in order to perform an efficient polarization rotation, the component's vertical symmetry must be broken, which can be observed in conventional silicon polarization rotators [2]. This comes from the fact that in 2 dimensions (that is to say when the optical indices are constant along the etching direction) TE and TM modes are entirely uncorrelated since (E_x, E_y, H_z) and (H_x, H_y, E_z) are solutions of two independent equations.

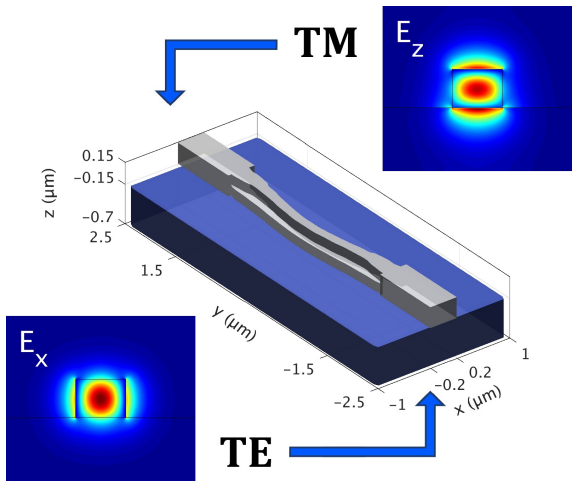


Fig. 1. Schematic of a two-level photonic polarization rotator.

From this observation we propose to derive a method allowing to find multi-levels photonic components using inverse design methods (Fig. 1). For this the optimization algorithm must obtain a design respecting the constraint that the top level is always supported by the bottom one. We develop in the following the mathematical and numerical aspects of the multi-level shape optimization prior to a quantitative comparison of single and two-level shaped polarization rotators. Optimized performances in terms of insertion losses and polarization conversion efficiency are finally illustrated with consistent results on three commercial software.

2. MATHEMATICAL & NUMERICAL ASPECTS

A. Shape optimization

Shape optimization (also known as inverse design) is a set of mathematical tools allowing to automatically determine the design of a device or optimize an existing one in order to maximize a given figure of merit. Several shape optimization methods have been used in the context of nanophotonics [7]. Among them we can cite methods optimizing photonic devices with binary valued pixels like particle swarm or genetic algorithm [12–15], methods using a continuous relaxation of indices values as in [16–18] or also level-set based algorithm [8, 19, 20]. In this paper we focus on geometrical optimization based on Hadamard's shape derivative concept as in [20] which we briefly describe in the next section.

B. Hadamard's shape derivative

Throughout this section we identify the shape of the component by means of a set $\Omega \subset \mathbb{R}^2$. In other words, for every point $\boldsymbol{x} \in \mathbb{R}^3$, the optical index is equal to the one of the silicon if and only if $\boldsymbol{x} \in \Omega \times [0, d]$ where d is the etching depth.

We will also denote by $\mathcal{J}(\Omega)$ the figure of merit that we wish to maximize. In the case of a TE $\rightarrow$ TM polarization rotator we need to maximize the amount of power carried by the fundamental (normalized) TM mode $(\boldsymbol{E}_{\mathrm{TM},0}, \boldsymbol{H}_{\mathrm{TM},0})$ in the output port Γ_{out}. This is equivalent to define $\mathcal{J}$ as the following overlap integral:

$$\mathcal{J}(\Omega) = \left| \frac{1}{4} \int_{\Gamma_{\mathrm{out}}} \left[\boldsymbol{E}_\Omega \times \boldsymbol{H}^*_{\mathrm{TM},0} + \boldsymbol{H}_\Omega \times \boldsymbol{E}^*_{\mathrm{TM},0} \right] \cdot \widehat{\boldsymbol{y}}\, ds \right|^2 \qquad (1)$$

where $(\boldsymbol{E}_\Omega, \boldsymbol{H}_\Omega)$ corresponds to the electromagnetic field obtained by injecting the fundamental TE mode through the input port Γ_{in} and using the optical index given by Ω.

To optimize $\mathcal{J}$, the idea behind Hadamard's method consists in an iterative modification of Ω into $\Omega_{\boldsymbol{\theta}} = \{\boldsymbol{x} + \boldsymbol{\theta}(\boldsymbol{x}), \boldsymbol{x} \in \Omega\}$ using a small vector field $\boldsymbol{\theta} : \mathbb{R}^3 \rightarrow \mathbb{R}^3$. In order to find the optimal vector field $\boldsymbol{\theta}$ to consider we need to study the sensibility of the application $\boldsymbol{\theta} \mapsto \mathcal{J}(\Omega_{\boldsymbol{\theta}})$. For most figure of merits, differentiating this expression at 0 gives rises to the following first order expansion, valid for any smooth $\boldsymbol{\theta}$

$$\mathcal{J}(\Omega_{\boldsymbol{\theta}}) = \mathcal{J}(\Omega) + \left\langle \mathcal{J}'(\Omega), \boldsymbol{\theta} \right\rangle_{\partial\Omega} + o(\boldsymbol{\theta}) \qquad (2)$$

where $\langle \cdot, \cdot \rangle_{\partial\Omega}$ stand for the L^2 scalar product on the border of the shape $\partial\Omega$ and $\mathcal{J}'(\Omega) : \mathbb{R}^3 \rightarrow \mathbb{R}^3$ is refered as the shape derivative of the functional $\mathcal{J}$. Taking $\boldsymbol{\theta} = \eta \mathcal{J}'(\Omega)$ in Eq. (2) with η sufficiently small automatically implies that $\mathcal{J}(\Omega_{\boldsymbol{\theta}})$ is greater than $\mathcal{J}(\Omega)$ and thus a new design shape $\Omega_{\boldsymbol{\theta}}$ better than the one using Ω is found. Again for most figure of merits the shape derivative is given explicitly by [20, 21]:

$$\mathcal{J}'(\Omega) = \vec{\boldsymbol{n}}_\Omega\, k^2 \int_0^d \mathcal{R}e \Big[(n^2_{\mathrm{Si}} - n^2_{\mathrm{Air}}) \boldsymbol{E}_{\Omega,\parallel} \cdot \boldsymbol{A}^*_{\Omega,\parallel} - (n^{-2}_{\mathrm{Si}} - n^{-2}_{\mathrm{Air}}) n^2_\Omega \boldsymbol{E}_{\Omega,\perp} n^2_\Omega \boldsymbol{A}^*_{\Omega,\perp} \Big]\, dz \qquad (3)$$

where $\boldsymbol{A}_\Omega$ is an adjoint solution (defined below) and $\vec{\boldsymbol{n}}_\Omega$ the normal vector orthogonal to Ω. In the case of Eq. (1), $\boldsymbol{A}_\Omega$ is given by solving Maxwell's equations with the TM mode coming from Γ_{out} multiplied by $-\left(\int_{\Gamma_{\mathrm{out}}} \boldsymbol{E}_\Omega \times \boldsymbol{H}^*_{\mathrm{TM},0} \cdot \widehat{\boldsymbol{y}}\, ds \right)^* / (4i\omega\mu_0)$.

To summarize, the optimization algorithm consists of a main loop following 3 steps:

1. *(simulations)* Compute the electric fields $\boldsymbol{E}_\Omega$ and $\boldsymbol{A}_\Omega$.
2. Compute the shape derivative given by Eq. (3).
3. *(gradient descent)* Compute the new shape $\Omega_{\eta\mathcal{J}'(\Omega)}$.

Note here that step (3) is performed using the level-set method [22]. In a nutshell this method associates a shape Ω with a function $\phi : \mathbb{R}^2 \rightarrow \mathbb{R}$ (the level-set function) such that $\Omega = \{\boldsymbol{x}, \phi_\Omega(\boldsymbol{x}) < 0\}$. Using this representation, $\phi_{\Omega_{\eta\mathcal{J}'(\Omega)}}$ (a level-set function associated to $\Omega_{\eta\mathcal{J}'(\Omega)}$) may be found solving an Hamilton-Jacobi equation (see for instance [22, 23]).

We now present a way to manage multi-levels optimization. Without loss of generality we will only deal here with the particular case of two etching levels. Thus the device's shape is now given by two shapes $\Omega_{\mathrm{top}}, \Omega_{\mathrm{bottom}} \subset \mathbb{R}^2$ with the constraint that Ω_{top} must be included in Ω_{bottom}. In order to fullfil such constraint, we use a projected gradient descent algorithm exploiting the level-set representation of the shapes. That is to say we add a fourth step (4) to impose the top level-set as the maximum between the two level-sets, or mathematically:

$$\phi_{\mathrm{top}}(\boldsymbol{x}) = \max\left(\phi_{\mathrm{bottom}}(\boldsymbol{x}), \phi_{\mathrm{top}}(\boldsymbol{x}) \right). \qquad (4)$$

Such algorithm gives priority to the bottom level over the top one, even though the reciprocal case could be considered.

C. Numerical solution of Maxwell equations

At each iterations of the optimization algorithm we need to solve Maxwell's equations injecting both the fundamental TE mode inside Γ_{in} to find $\boldsymbol{E}_\Omega$ and the fundamental TM mode inside Γ_{out} to find $\boldsymbol{A}_\Omega$. To do this we used a `Matlab` (The MathWorks, Inc., Natick, U.S.A.) script calling the `RSoft Photonics` (RSoft Design Group, Inc., New York, U.S.A) commercial solver in a loop. The computational domain is discretized using a 3 µm $\times$ $(L + 2)$ µm $\times$ 2 µm wide grid (with L the length of the polarization rotator) regularly spaced with spatial steps of 25 nm in each directions and surrounded by perfectly matched layers. A simulation result of the electric field can be observed in Fig. 2.

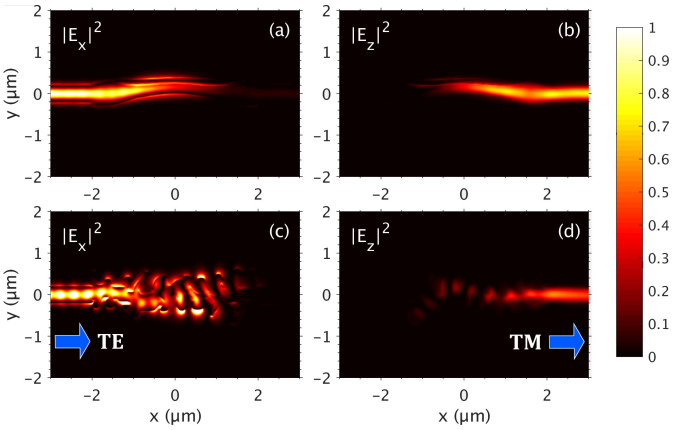


Fig. 2. Slice of the electric field at $z = 0$ showing polarization rotation. (a),(b) two-levels design (c),(d) one-level design. FDTD (Finite Difference Time Domain) simulations at $\lambda = 1.55$ µm.

In the next section we validate our numerical method by shape optimizing a TE $\rightarrow$ TM polarization rotator operating at

$\lambda = 1.55$ µm using one or two levels of etching in a 300 nm silicon layer mounted on a silica substrate. For the two-levels devices a partial etching of half the silicon layer's height is considered. The refractive indices of both Si and SiO_2 are taken from the classical handbook of Palik [24].

3. APPLICATION TO POLARIZATION ROTATORS

A. Single and two-level optimization

Figure 3 depicts the optimization of a polarization rotator with a single level of etching (blue curve) and two levels of etching (orange curve) for an arbitrarily fixed length of 4 µm. For the single etched device, the optimization process requires more than 1000 iterations in order to reach sufficient convergence. It is worth noting that this device exhibits similar performances as the one demonstrated previously with binary shapes shown in [15], with about −1.9 dB (65 %) of transmission from TE to TM, even thought the two non intuitive design methods are different.

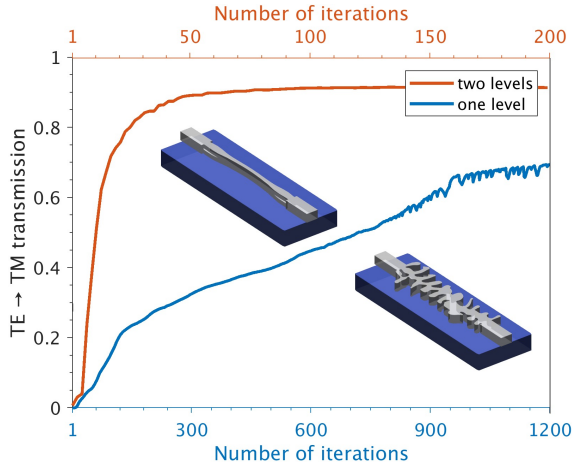


Fig. 3. Convergence graph of the figure of merit for the one and two levels 4 µm polarization rotators (notice the two differents x-axis). One iteration corresponds to $\sim$ 10 minutes of computation using a 20 cores 3 Ghz CPU.

On the other hand, the two-level device optimization reaches rapidly a plateau after 100 iterations (10× computation time reduction), with a drastic improvement of the transmission greater than 90 % for the same compactness, thus confirming the necessity to break the vertical invariance.

The performances of the two devices can be furthermore compared by plotting the transmission as a function of the wavelength for both the TE to TM conversion and the undesired TE to TE residual transmission, as shown in Fig. 4(a).

While a relatively small TE to TM conversion bandwidth is found for the single level shape device (blue curve of Fig. 4(a)), the TE to TM polarization conversion of the two-level component presents more than 85 % conversion in a 100 nm bandwidth (orange curve). The impact on the Polarization Conversion Efficiency (PCE) can be observed in the Fig. 4(b) with again a broadband operation for the multi-level optimization with a $PCE > 97$ %, the PCE being defined as $PCE = P_{TM}/(P_{TE} + P_{TM})$ where P_{TE} and P_{TM} corresponds to the power exiting the device for each polarization (see Eq. (1) for TM). Although excellent performances were obtained from this first two-level optimization with a 4 µm × 1 µm footprint, we investigate finally the influence of the device length for the same two-level optimization and consolidate our conclusions by comparing the calculations with different numerical tools.

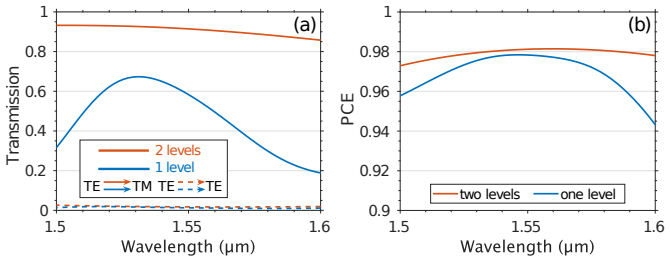


Fig. 4. Comparison of both transmission (a) and polarization conversion efficiency (b) between the one and two levels 4 µm length designs.

B. Efficiency and compactness

The transmission of two-levels optimized polarization as a function of the length is shown in the Figure 5. For this comparison, the same initialization was chosen (straight waveguide) and the convergence was stopped equally after 200 iterations.

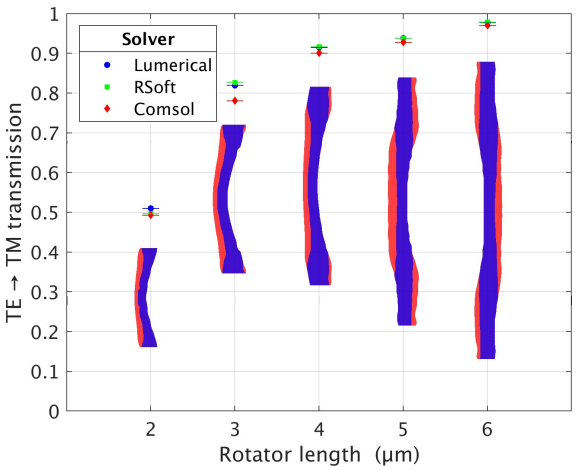


Fig. 5. Transmission of two-levels polarization rotators from 2 µm to 6 µm in length. Each device is represented in red (bottom level) and blue (top level).

In order to increase the confidence in our numerical results a comparison between three different numerical softwares was additionally performed, namely `Lumerical` (Lumerical Solutions, Inc., Vancouver, Canada) and `RSoft Photonics` using 3D-FDTD as well as `Comsol Multiphysics` (COMSOL AB, Stockholm, Sweden) using 3D-FEM (Finite Element Method). The computational domain discretization on all three software has been chosen so that the edges of the elements are of at most $\lambda/(10 \times n)$ nm, and boundary conditions were also assigned similarly with perfectly matched layers. The resulting transmissions are displayed in the Fig. 5 with colored dots revealing a high consistency between the two FDTD solvers. The FEM transmission values are also in good agreement with FDTD, showing the same behavior as a function as the length, with a transmission higher than 95 % for the 6 µm long device.

The transmission as a function of the wavelength is shown in Fig. 6(a) for polarization rotator length ranging from 3 µm

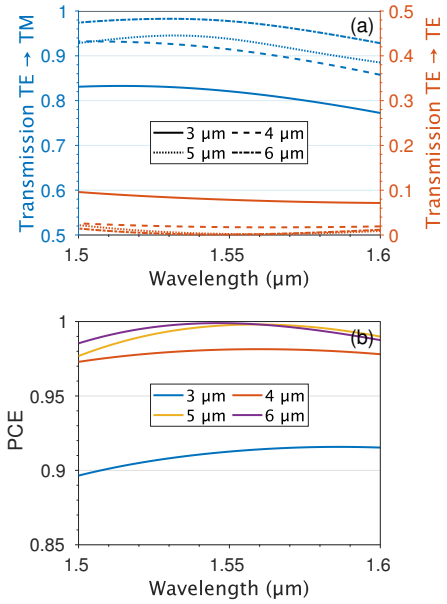


Fig. 6. (a) Transmission into TM and TE polarizations inside the output waveguide for each two-levels designs, (b) corresponding polarization conversion efficiency.

to 6 μm. A clear improvement of the insertion losses can be seen from the blue curves when increasing the length, down to $\simeq -0.2$ dB (95 %), whereas the residual TE transmissions remains constant after 5 μm. This fact can be readily seen on the polarization conversion efficiency plot of Fig. 6(b), for which the broadband capability of our two-levels designs is displayed.

Table 1 summarizes the performances of the two-level shape-optimized silicon photonic polarization converter, and compares it to numerically and/or experimentally demonstrated compact designs. We have selected a variety of works representing either conventional [2], shape optimized [12, 15] and plasmonic [10] compact devices which are of interest for this comparison. This table not only shows the insertion loss (IL) and the PCE but also the Extinction Ratio (ER) defined in dB as $10\log_{10}(P_{\mathrm{TM}}/P_{\mathrm{TE}})$.

	Ref. [2]	Ref. [12]	Ref. [15]	Ref. [10]	This work
	e.	n./e.	n./e.	n.	n.
IL (dB)	0.51	0.7/2.5	3/4.3	2.1	0.33
ER (dB)	9.5	15/10	23/9	14	> 30
PCE (%)	88.9	96.9/90.9	99.5/88.7	~ 96	> 98.5
Length (μm)	6	4.2	5	5	6
BW (nm)	80	157/140*	40	–	100

* -1 *dB bandwidth*

Table 1. Comparison of numerical (n.) and/or experimental (e.) works on a selection of polarization rotators found in the literature. (BW) stands for bandwidth.

The numerical quantification of our work shows an improvement in the insertion losses for a similar compactness and extinction ratio, although an experimental demonstration must be performed in the future to validate this study.

4. CONCLUSION

In summary, we proposed an algorithm to integrate multi-level shape optimization inside classical adjoint-based geometrical methods. This algorithm was implemented for the design of an efficient and ultra-compact silicon polarization rotator. The performances were compared to single level shape optimized device and to the literature, showing potential state of the art performances evaluated numerically. The numerical results were subsequently challenged on three commercial calculation tools, the results are found in excellent agreement, which provide a high confidence on the expected performances when the device will be fabricated. The robustness to fabrication variations and manufacturing should be studied in a future work, using for instance the methods presented in [19, 20]. On the mathematical side, an interesting development would be to no longer resort on a projection-based method as in section 2.A giving priority to one of the two levels but rather consider the best common descent direction satisfying the inclusion constraint.

5. ACKNOWLEDGMENT

The authors thank Pr. E. Oudet and Dr. C. Dapogny for their valuable help in the mathematical and numerical optimization work.

REFERENCES

1. L. Chen, C. R. Doerr, and Y.-K. Chen, Opt. Lett. **36**, 469 (2011).
2. D. Vermeulen, S. Selvaraja, P. Verheyen, P. Absil, W. Bogaerts, D. Van Thourhout, and G. Roelkens, IEEE Photonics Technol. Lett. **24**, 482 (2012).
3. H. Xu and Y. Shi, Opt. letters **42**, 771 (2017).
4. S. Dwivedi, H. D'heer, and W. Bogaerts, IEEE Photonics Technol. Lett. **25**, 2167 (2013).
5. N. Matsuda, H. Le Jeannic, H. Fukuda, T. Tsuchizawa, W. J. Munro, K. Shimizu, K. Yamada, Y. Tokura, and H. Takesue, Sci. reports **2**, 817 (2012).
6. M. Hochberg and T. Baehr-Jones, Nat. photonics **4**, 492 (2010).
7. S. Molesky, Z. Lin, A. Y. Piggott, W. Jin, J. Vucković, and A. W. Rodriguez, Nat. Photonics **12**, 659 (2018).
8. C. M. Lalau-Keraly, S. Bhargava, O. D. Miller, and E. Yablonovitch, Opt. express **21**, 21693 (2013).
9. J. Huang, J. Yang, D. Chen, X. He, Y. Han, J. Zhang, and Z. Zhang, Photonics Res. **6**, 574 (2018).
10. J. N. Caspers, M. Alam, and M. Mojahedi, Opt. letters **37**, 4615 (2012).
11. K. Hassan, F. Leroy, G. Colas-des Francs, and J.-C. Weeber, Opt. letters **39**, 697 (2014).
12. Z. Yu, H. Cui, and X. Sun, Opt. letters **42**, 3093 (2017).
13. B. Shen, P. Wang, R. Polson, and R. Menon, Nat. Photonics **9**, 378 (2015).
14. J. C. Mak, C. Sideris, J. Jeong, A. Hajimiri, and J. K. Poon, Opt. letters **41**, 3868 (2016).
15. A. Majumder, B. Shen, R. Polson, and R. Menon, Opt. express **25**, 19721 (2017).
16. J. S. Jensen and O. Sigmund, Laser & Photonics Rev. **5**, 308 (2011).
17. J. Lu and J. Vučković, Opt. express **21**, 13351 (2013).
18. Y. Elesin, B. S. Lazarov, J. S. Jensen, and O. Sigmund, Photonics Nanostructures-Fundamentals Appl. **12**, 23 (2014).
19. A. Y. Piggott, J. Petykiewicz, L. Su, and J. Vučković, Sci. reports **7**, 1786 (2017).
20. N. Lebbe, C. Dapogny, E. Oudet, K. Hassan, and A. Gliere, "Robust shape and topology optimization of nanophotonic devices using the level set method," (2018). HAL preprint hal-01860882, URL https://hal.archives-ouvertes.fr/hal-01860882.
21. S. G. Johnson, M. Ibanescu, M. Skorobogatiy, O. Weisberg, J. Joannopoulos, and Y. Fink, Phys. review E **65**, 066611 (2002).
22. S. Osher and R. Fedkiw, *Level set methods and dynamic implicit surfaces*, vol. 153 (Springer Science & Business Media, 2006).
23. S. Osher and J. A. Sethian, J. computational physics **79**, 12 (1988).
24. E. D. Palik, *Handbook of optical constants of solids*, vol. 3 (Academic press, 1998).